Chapter 6

Experimental results and discussions

6.1 Introduction

In the previous chapter the steady state stability analysis of the proposed controller has been analysed. The controller has been found to be stable invarient to the operating point of the wind turbine torque-speed characteristics. In present chapter the experimentations on the hardware setup have been conducted to comment on the following criteria:

1. Effect of proposed controller on the performance of the wind generator

2. Effectiveness of the proposed RWECS under variable wind conditions and supplying constant load

3. Effectiveness of the proposed RWECS under constant wind and supplying variable load

4. Low-voltage-ride-through (LVRT) capability of the proposed system

6.2 Effect of the proposed controller on the performance of the wind generator

Section 2.4 and section 4.1 presents the advantages and suitability of using the MFW-based voltage regulation technique to a DSAF PMSG generator. However, the type of DSAF PMSG generator best suited for the MFW-based voltage regulation technique has not yet been reported.

PM generators are categorized based on their back-EMF characteristics into brushless dc (BLDC) and synchronous generator (PMSG). BLDC machine has trapezoidal back-EMF while, PMSG has sinusoidal back-EMF characteristics. In this section, both types of machines have been compared for voltage regulation by the MFW technique.

The four configurations of DSAF PMSG, namely topology T1, T2, T3 (already detailed in chapter 3), and one BLDC (T4) (simulated) have been compared to test the effects of MFW on the performance of the generator. As detailed before, T1 comprises of two pancake-shaped toroidal-core stators made of CRGO steel. PM on the rotor is full-pitched. Due to the absence of the inter-polar regions, the back-EMF waveform has high-peak sinusoidal, as shown in Fig. 6.1 (a).

Topology T2 is similar in construction to T1. The only difference is the rotor. PM on the rotor is fractional-pitched, resulting in smooth sinusoidal back-EMF waveform [147]. Fig. 6.2 (a) provides the back-EMF waveform of T2 topology. However, the presence of teeth on the stator modulates the back-EMF waveform and generate cogging torque in the generator. Therefore, a core-less machine, Topology T3, is constructed with the same design parameters as in T2. The back-EMF waveform is again a smooth sinusoidal free of any modulations. Fig. 6.3 (a) shows the back-EMF waveform of topology T3. Table 3.1 tabulates other design parameters of all the topologies.

On the other hand, T4 has a trapezoidal back-EMF characteristic that is simulated on MATLAB Simulink with 140^o electrical magnet arc-length. Fig. 6.4 shows the back-EMF waveform characteristic.

Experimental tests compare the performance of the MFW-based voltage regulation technique on generator topologies T1, T2, T3, and T4. MFW technique has been applied on three generator topologies, namely T1, T2, and T3, practically, and on a BLDC generator (Topology T3) in MATLAB Simulink.

Fig. 6.1 (a), 6.2 (a), 6.3 (a) and 6.4 (a) present generator no-load line voltage waveforms with zero SDA, i.e., both stators aligned, for topologies T1, T2, T3, and T4 respectively. Specifically, in T1, upon increasing SDA, dips in the line voltage waveform were prominent, as shown in Fig. 6.1 (b) and 6.1 (c). These dips are due to the HPS back-EMF characteristic in the topology. Higher the SDA higher the dips observed. On the other hand, no distortions have been observed in T2 and T3 topologies upon an increase in SDA, as shown in Fig. 6.2 and 6.3 owing to near-to-sinusoidal back-EMF characteristic. However, the distortion in T2 increases owing to increased modulation of air-gap magnetic field upon increase in SDA. In topology T3, no distortions have been observed upon an increase in SDA, and the THD is below prescribed IEEE standards of 5 %.

Fig. 6.4 (a), Fig. 6.4 (b) and Fig. 6.4 (c) shows simulated no-load line voltage waveform of BLDC generator at SDA= 0^o, 75^o, and 115^o electrical, respectively. The waveform distortions are most pronounced in the BLDC machine upon an increase in SDA.

However, Fig. 6.5 shows the effective-voltage-regulation in all the topologies is nearly the same and invariant to the voltage waveforms.

The Fast Fourier Transform (FFT) of the voltage waveform of each topology has been carried out to check and compare harmonic content in the same. Fig. 6.6 gives the comparison of FFT analysis of no-load voltage waveform in topologies T1, T3, and T4.

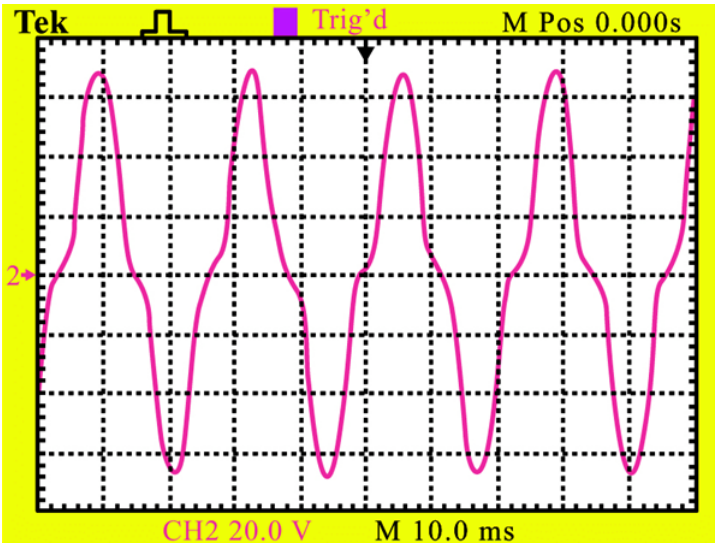

(a) Voltage waveform at stator displacement angle= 0^o electrical.

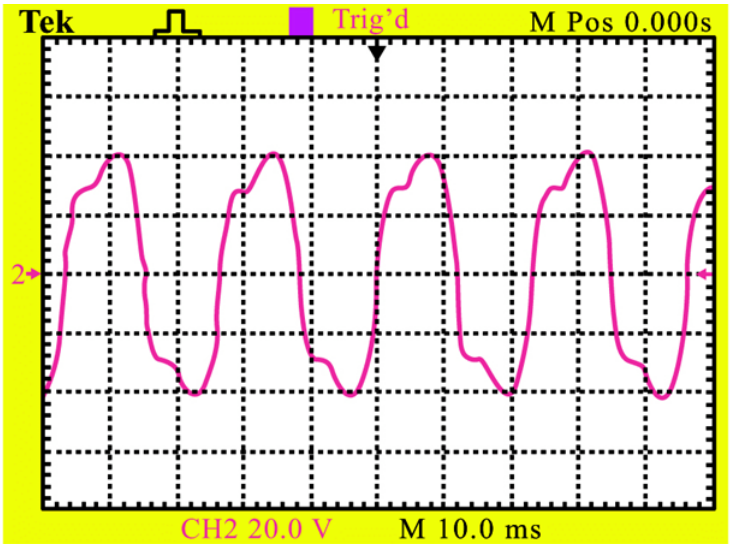

(b) Voltage waveform at stator displacement angle= 75^o electrical.

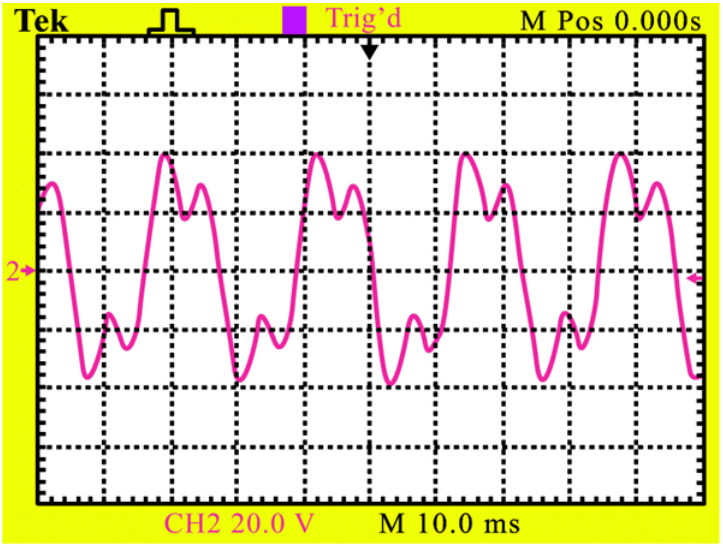

(c) Voltage waveform at stator displacement angle= 115^o electrical.

Fig. 6.1 Output no-load voltage waveform of Topology T1 at different stator displacement angles.

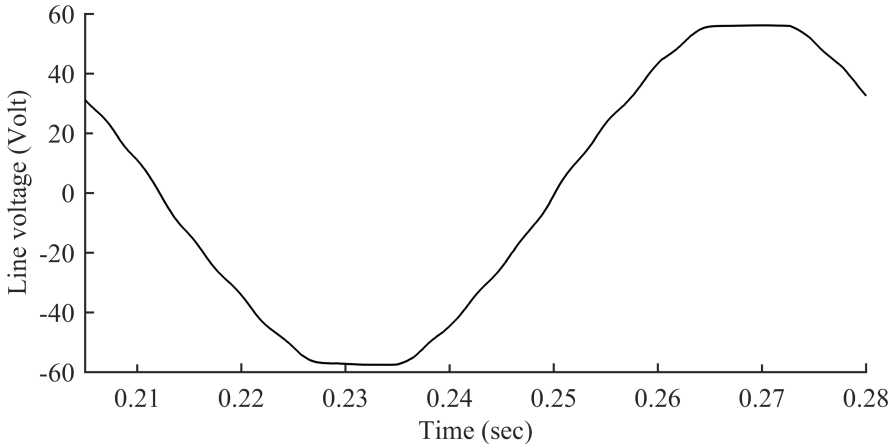

(a) Voltage waveform at stator displacement angle= 0^o electrical.

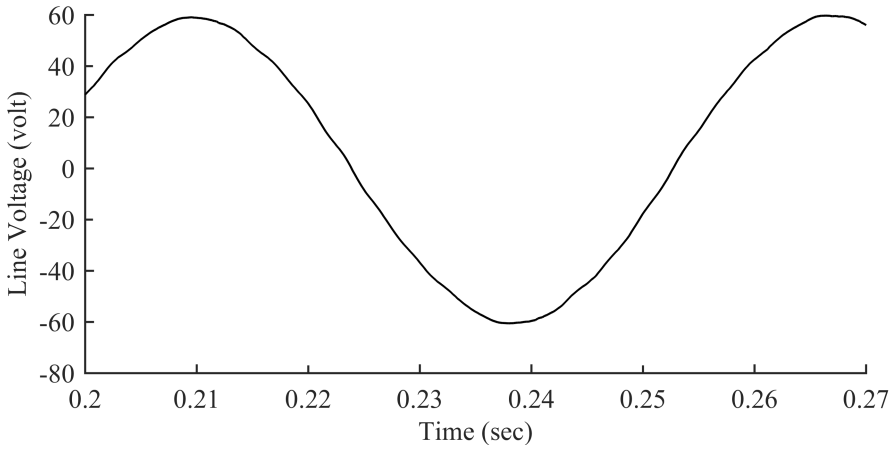

(b) Voltage waveform at stator displacement angle= 75^o electrical.

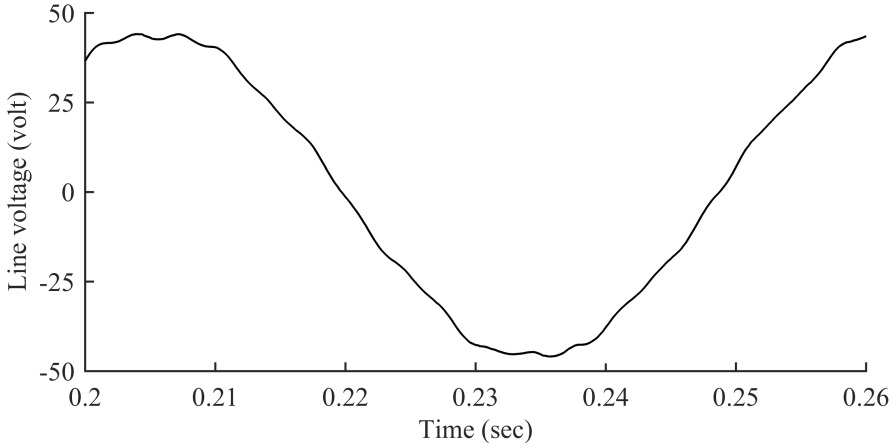

(c) Voltage waveform at stator displacement angle= 115^o electrical.

Fig. 6.2 Output no-load voltage waveform of Topology T2 at different stator displacement angles.

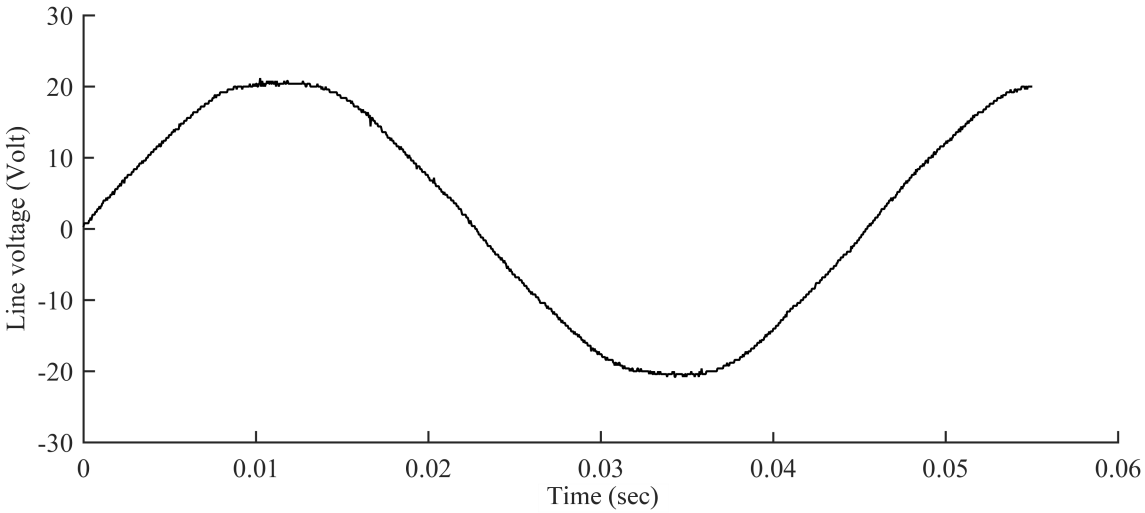

(a) Voltage waveform at stator displacement angle= 0^o electrical.

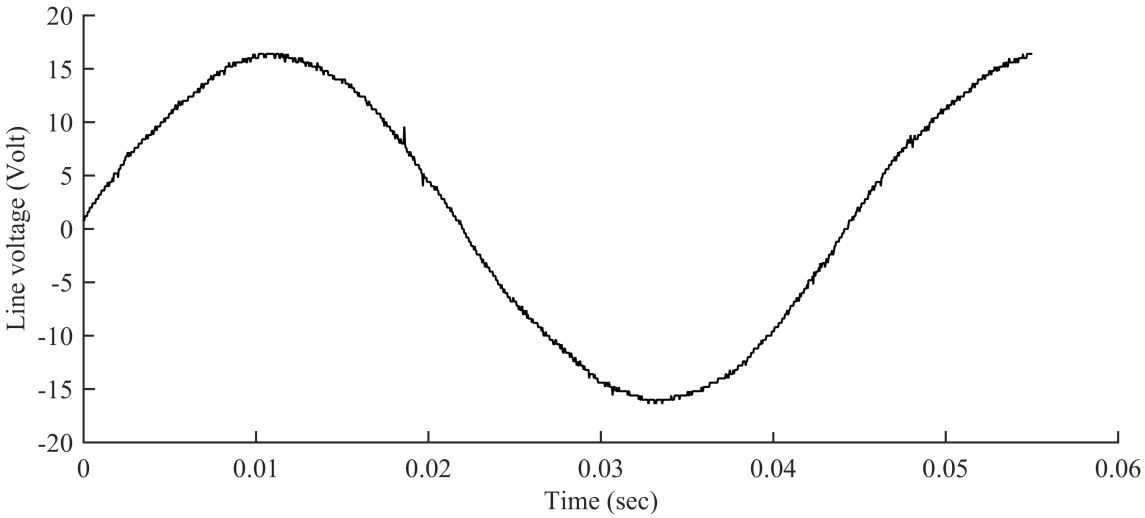

(b) Voltage waveform at stator displacement angle= 75^o electrical.

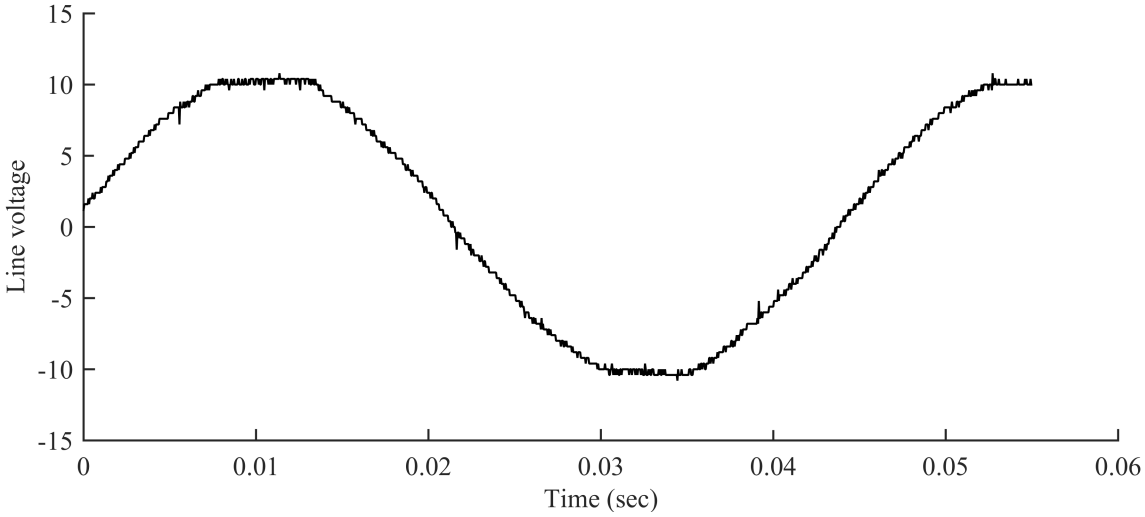

(c) Voltage waveform at stator displacement angle= 115^o electrical.

Fig. 6.3 Output no-load voltage waveform of Topology T3 at different stator displacement angles.

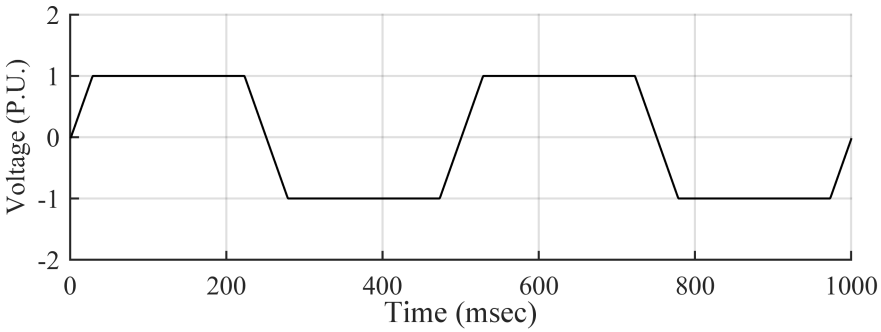

(a) Voltage waveform at stator displacement angle= 0^o electrical.

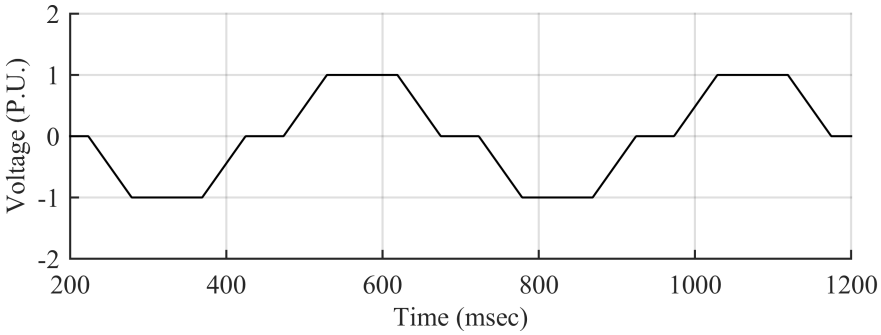

(b) Voltage waveform at stator displacement angle= 75^o electrical.

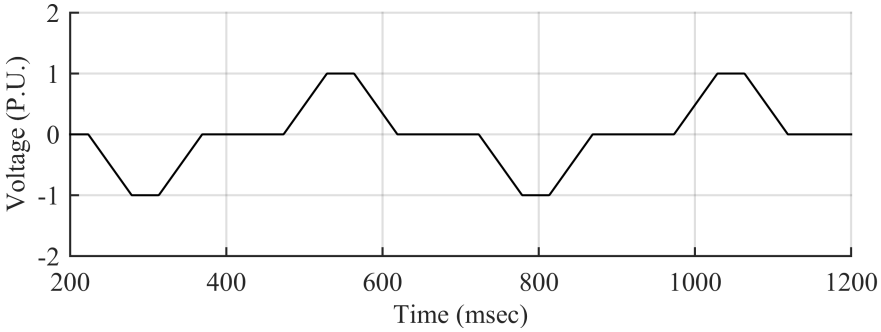

(c) Voltage waveform at stator displacement angle= 115^o electrical.

Fig. 6.4 Output no-load voltage waveform of Topology T4 at different stator displacement angles.

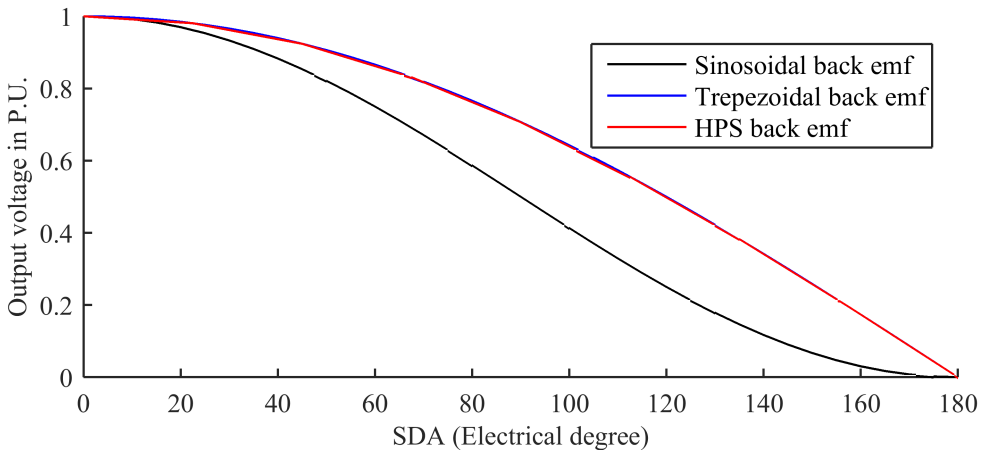

Fig. 6.5 Variations in Line voltage for trapezoidal, high peak sinusoidal, and near-to-sinusoidal back EMF characteristics as per angular shift of stator in electrical degree.

Topology T2 has been avoided from the analysis because T2 and T3 topology has similar back-EMF characteristics, and no-more information is expected from the analysis.

Higher harmonic contents have been observed in the BLDC generator owing to the trapezoidal air-gap flux density. Also, the harmonic contents in the BLDC generator is highly varying as per the variations in SDA. On the other hand, harmonics content in Topology T3 is low, and no substantial changes have been observed upon increasing SDA.

Moreover, THD for each topology has been estimated for different SDA and plotted in Fig. 6.7. Though it seems increasing SDA till 75^o electrical, THD of topologies T1 and T4 decreases. However, the drive circuitry becomes more complicated. The complexity increases owing to the need to incorporate the variations in the back-EMF waveform into the current profile to reduce the torque ripples in the generator. Thus, drive circuitry would not be the same as before, and its design is a subject matter of future research.

It is inferred from the above analysis that the effect of the MFW-based voltage regulation technique on the no-load performance of a near-to-perfect sinusoidal-back-EMF DSAF PMSG is minimum. Further, the same is tested at load. The performance of the generator at load again is diagnosed by FFT analysis of the line voltage waveform.

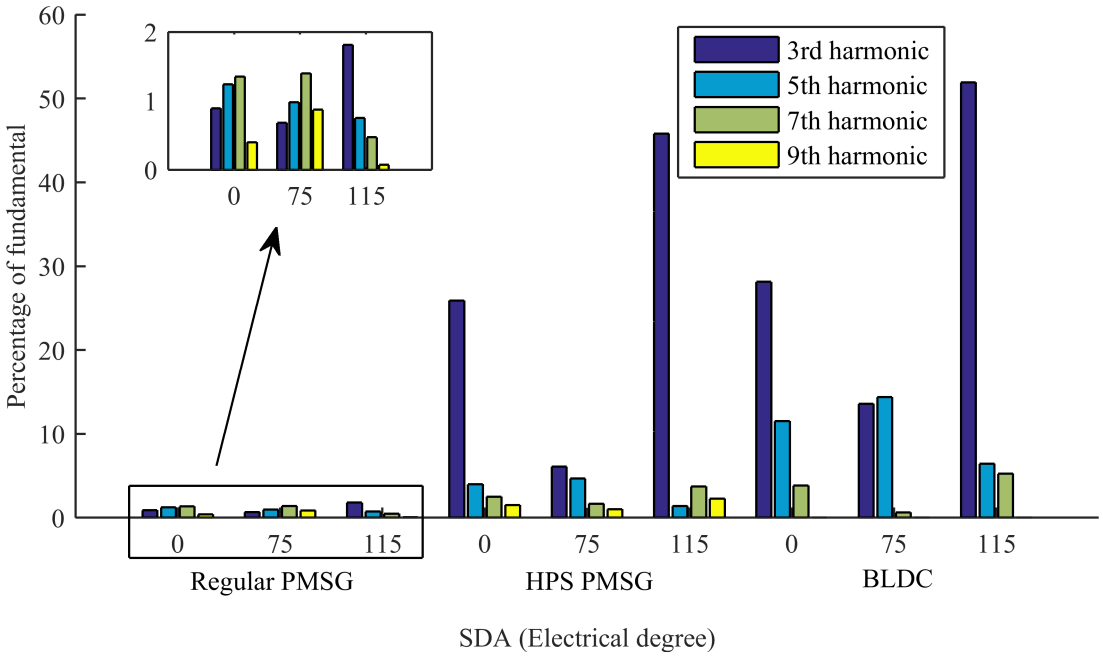

Fig. 6.6 Magnitude of different order of harmonics present in line voltage of different generator topologies upon increase in stator displacement angle.

For on-load testing, a three-phase diode rectifies the generator three-phase supply and then filtered by a DC-link capacitor. Subsequently, the rectified AC supply is connected across 10 ohm resistance. Fig. 6.9 shows DC-link voltage, DC load current, and generator line voltage waveform of T3 topology at SDA (a) 0^o (b) 75^o (c) 115^o electrical. Further, the FFT analysis of voltage waveforms is conducted, and subsequently, THD content is determined. Fig. 6.7 shows THD content in the generator line voltage at load at different SDA. In comparison with no-load results, an increase in THD content has been observed owing to the use of an uncontrolled rectifier.

Further, Fig. 6.8 shows the generator's current profile at SDA= 115^o electrical and its FFT analysis. The generator's current THD is higher when compared to generator line voltage THD. The higher generator current THD is due to the lower current harmonics injected into the generator owing to the use of an uncontrolled diode bridge rectifier at the generator end. The lower-order harmonics in the generator winding produce torque-ripples

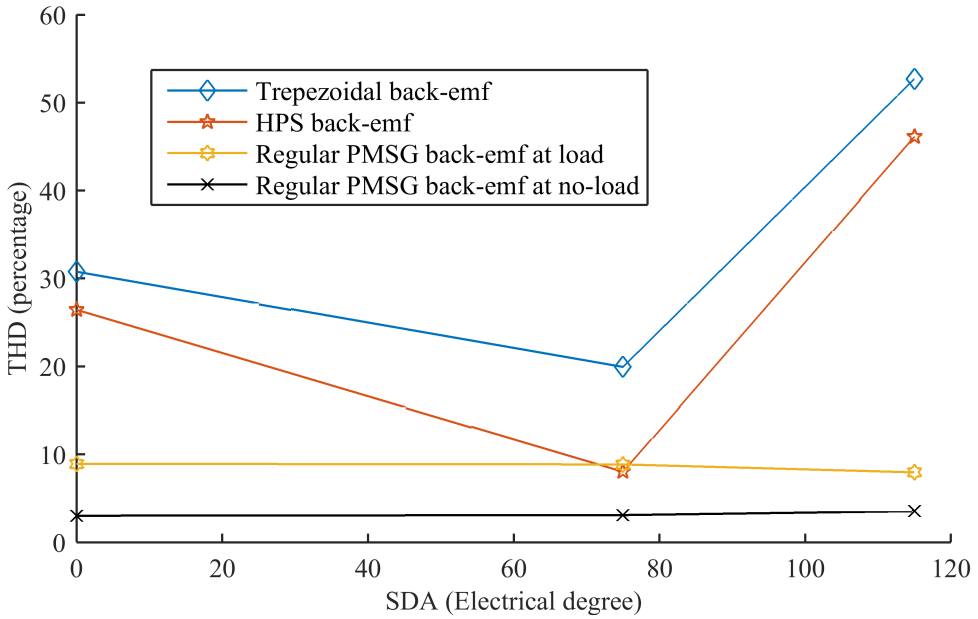

Fig. 6.7 THD content in line voltage of different generator topologies upon increase in stator displacement angle.

that could be detrimental to the generator shaft and the gearboxes, if any. However, the low-order harmonics could be easily filtered out using filters at the generator-end.

Similarly, load tests on topology T2 have been conducted, and results have been presented for analysis in Fig. 6.12, 6.13, and 6.14. It is concluded that the effect of MFW on the generator performance at load is nearly zero. Furthermore, THD decreases on increasing the SDA.

6.3 Performance of the proposed RWECS under variable wind conditions and constant load

The proposed RWECS is a dedicated system to counter high intermittent wind conditions at rooftop locations. For verifying the proposed hypothesis at variable wind speed and loads, the developed setup has been experimentally evaluated for

1. Variable wind speed supplying constant load.

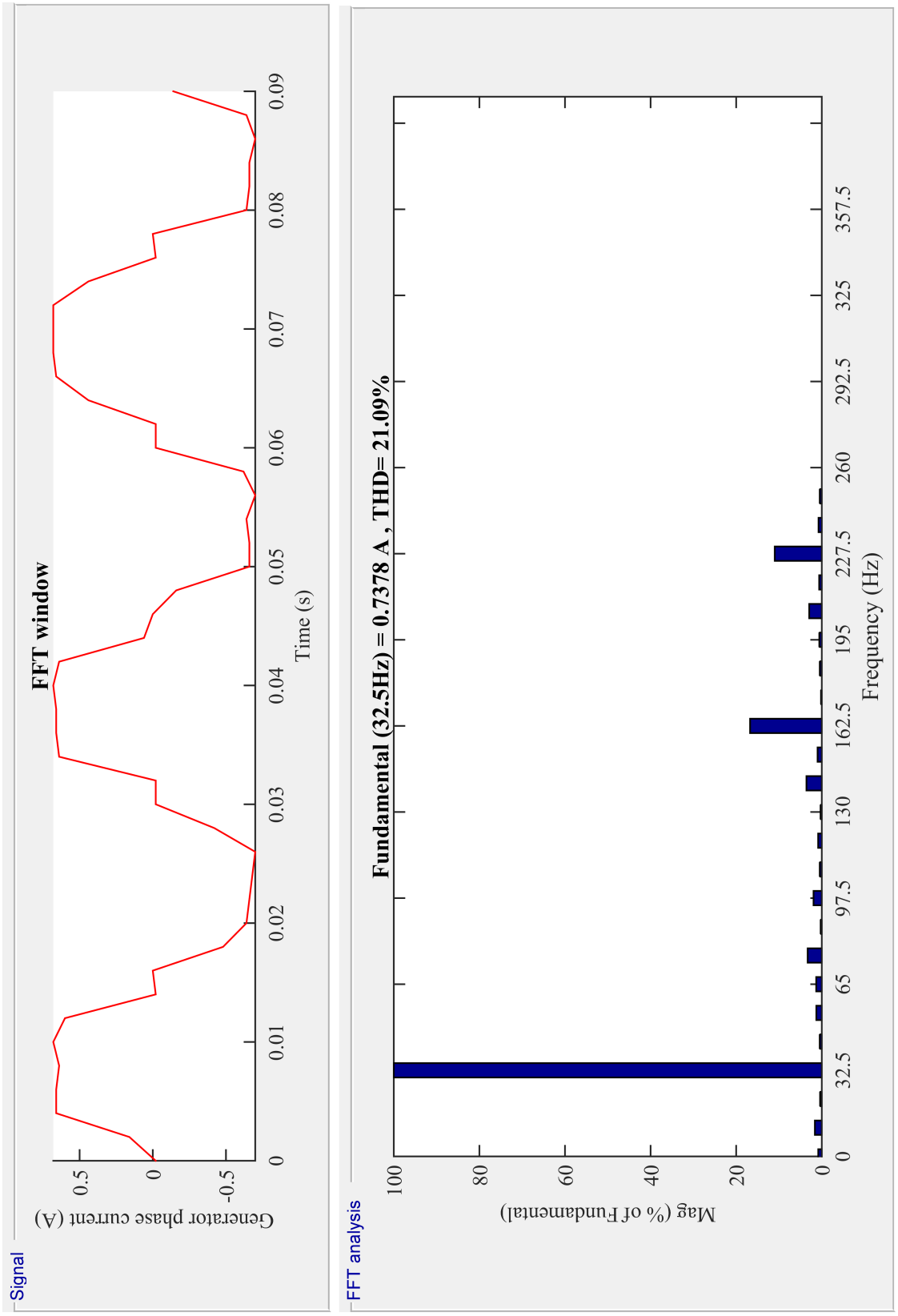

Fig. 6.8 FFT analysis of generator current profile of Topology T3 at $SDA = 115^{o}$.

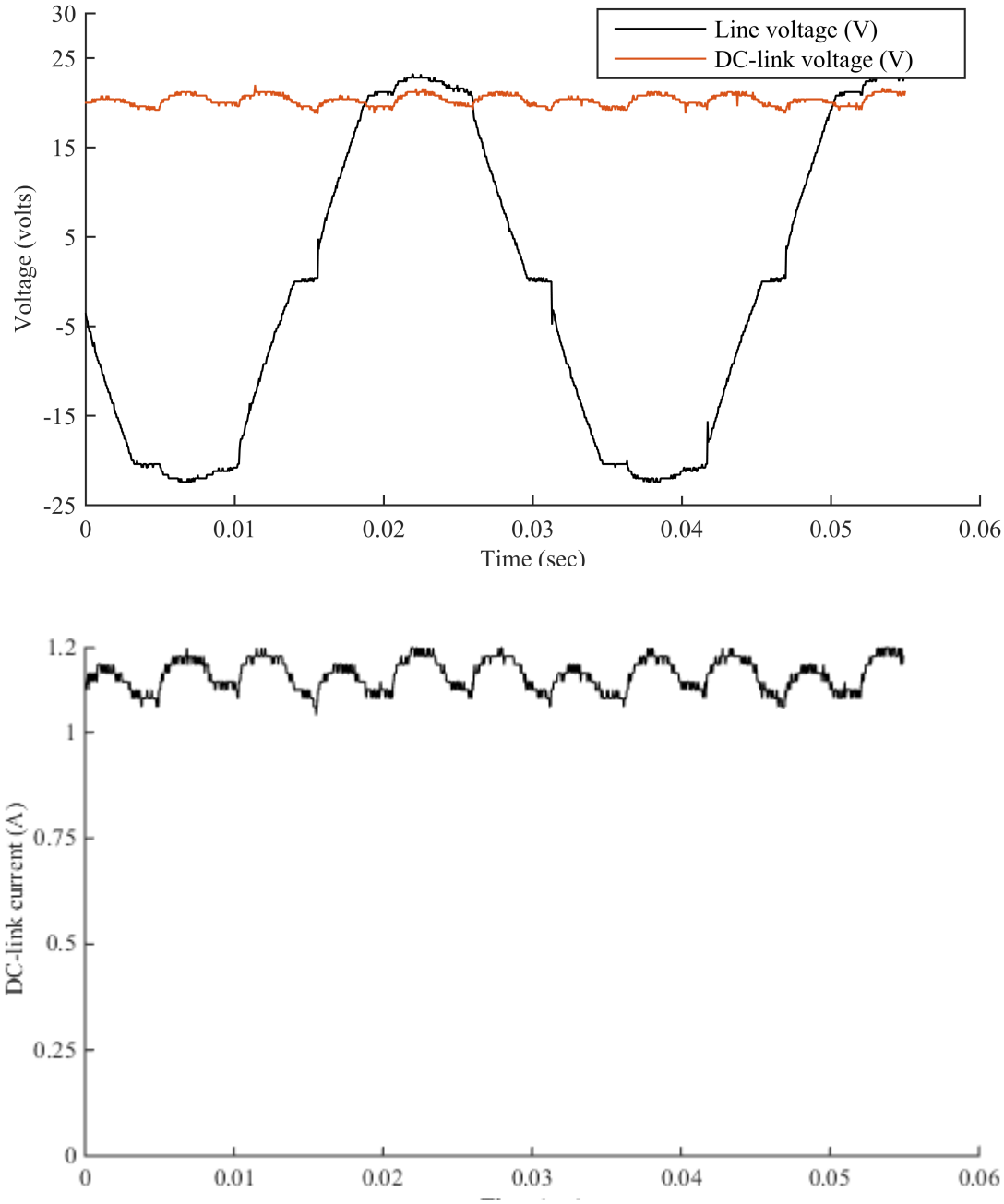

Fig. 6.9 Effect of mechanical field weakening in topology T3 at load at $SDA = 0^o$.

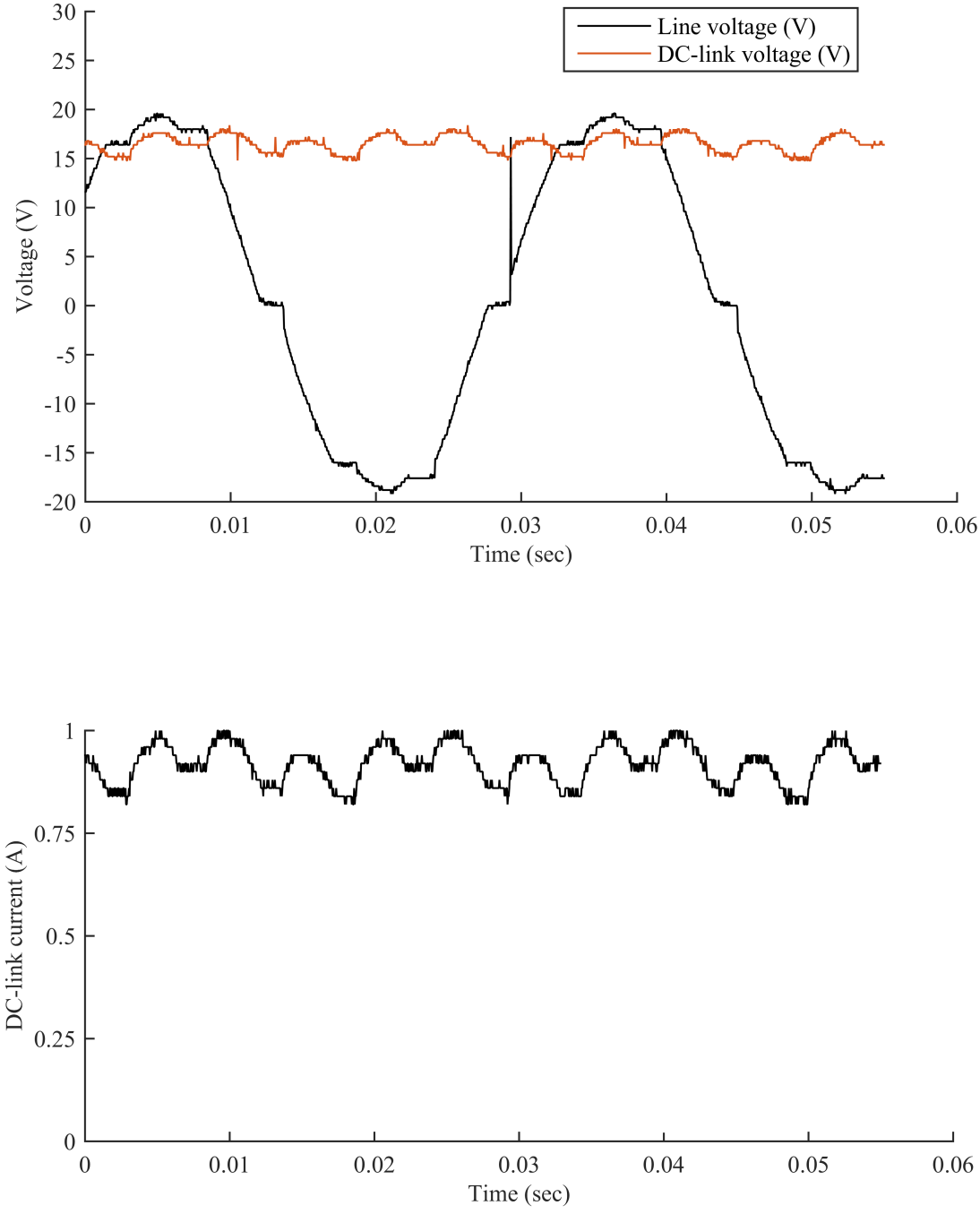

Fig. 6.10 Effect of mechanical field weakening in topology T3 at load at $SDA = 75^o$.

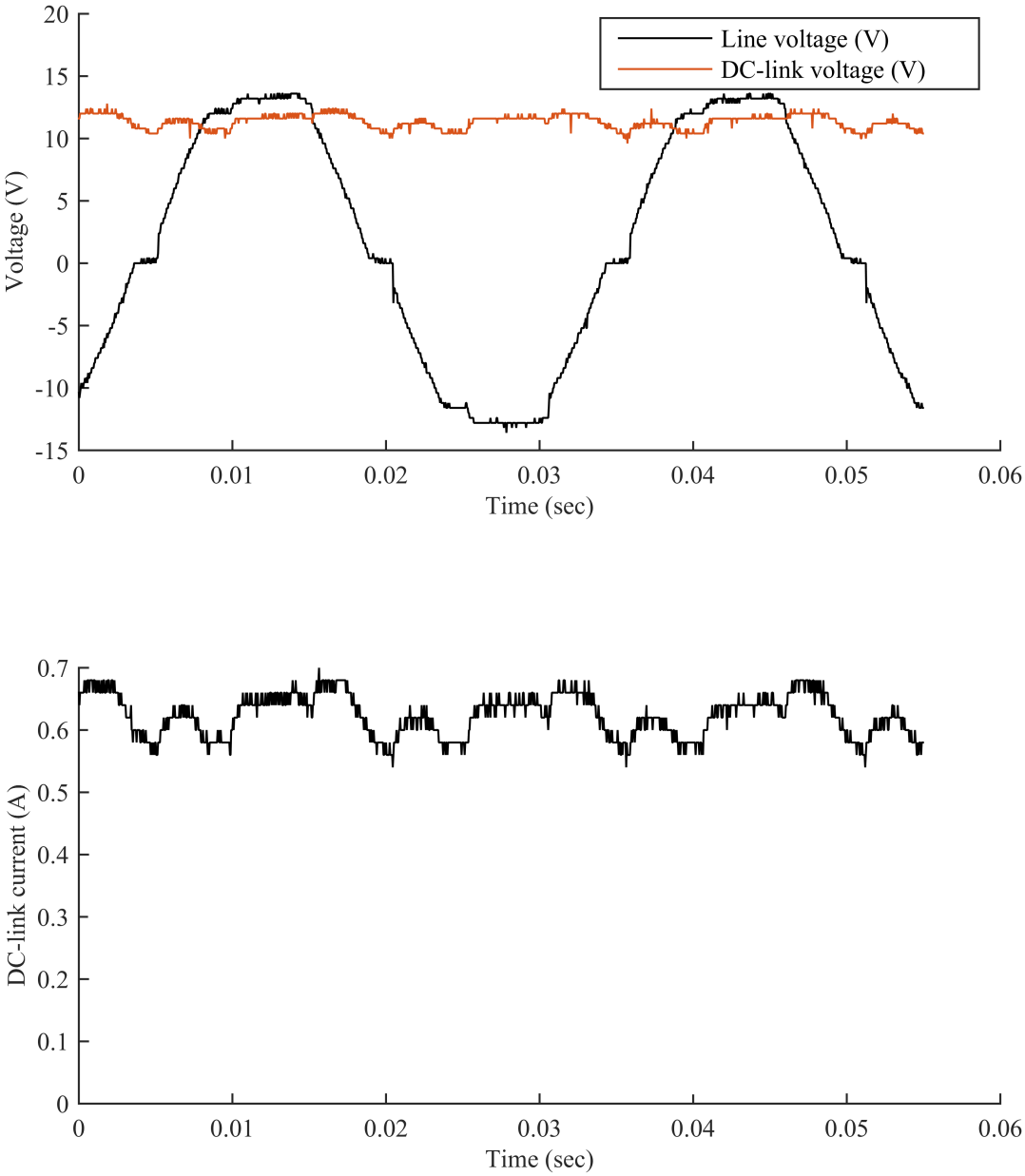

Fig. 6.11 Effect of mechanical field weakening in topology T3 at load at $SDA = 115^o$.

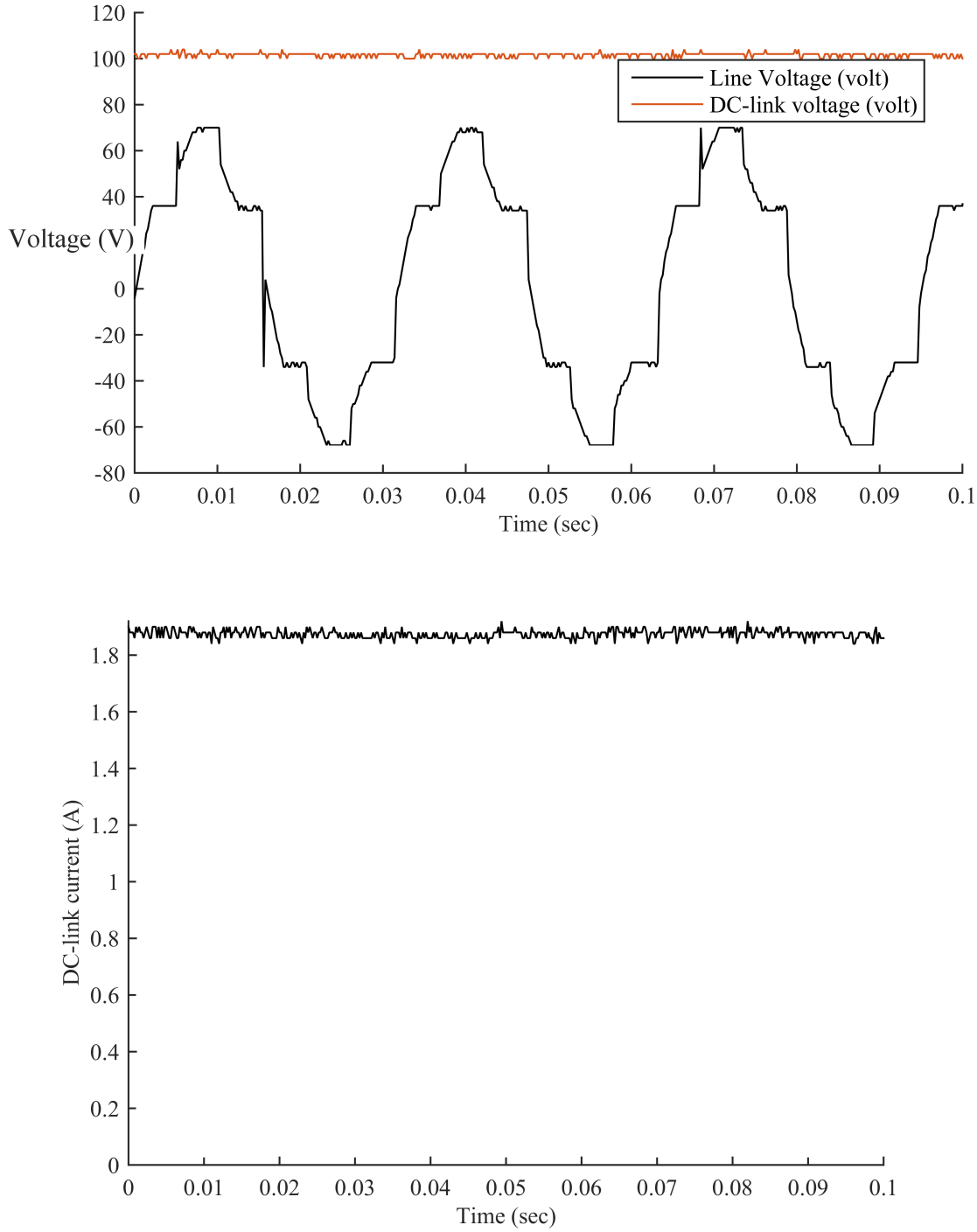

Fig. 6.12 Effect of mechanical field weakening in topology T2 at load at $SDA = 0^o$.

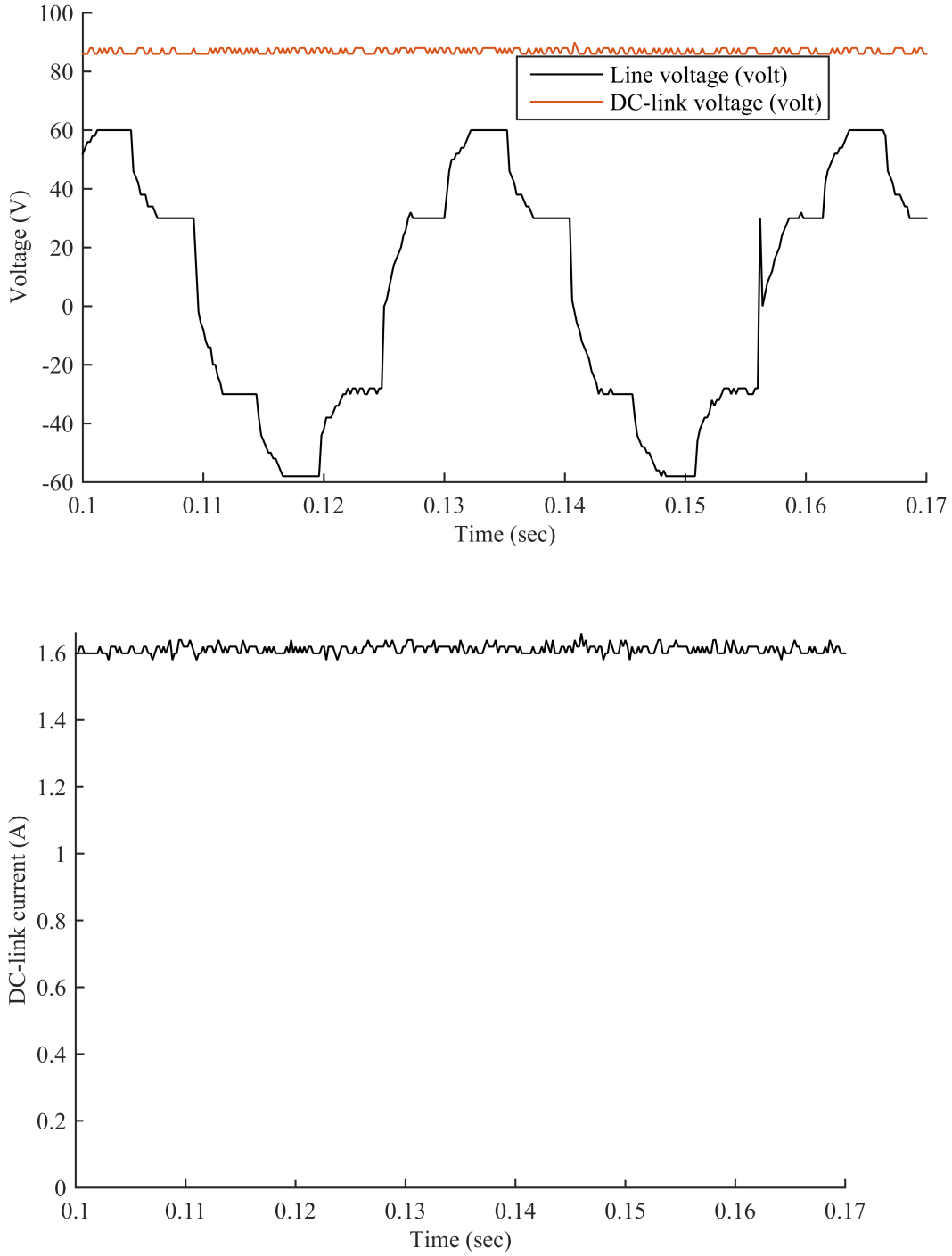

Fig. 6.13 Effect of mechanical field weakening in topology T2 at load at $SDA = 75^o$.

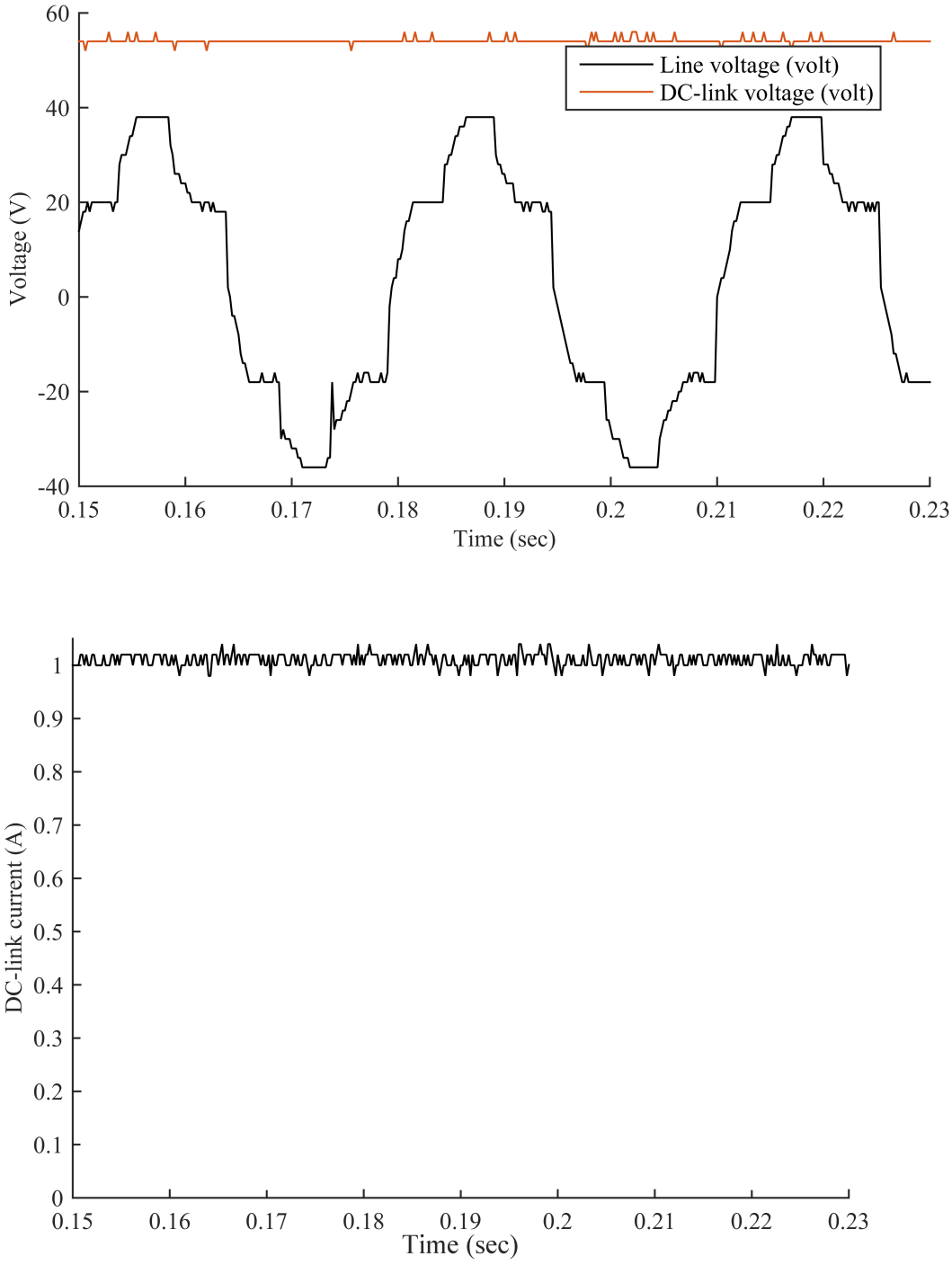

Fig. 6.14 Effect of mechanical field weakening in topology T2 at load at $SDA = 115^o$.

2. Constant wind speed supplying variable load.

Fig. 6.15 (a) presents a typical wind speed variations in time. Wind speed changes in steps to test the generator performance in the extreme conditions. In a practical system, the wind profile is smoother, and better performance of the system is expected. Fig. 6.15 (b) shows the load profile during the test. The loading of the generator has been reported in section 4.4. The tapping of the three-phase transformer has been fixed during the experiment and, therefore, operates at constant load. Fig. 6.15 (c) shows the dynamic change in SDA to maintain the DCV between ±10 percent of reference value as per Indian electrical code [148]. Fig. 6.15 (d) depicts the DCV profile as SDA changes. However, for lower tolerance of DCV, the frequency of RS increases, as reported in the next set of tests conducted on Constant wind and variable load conditions.

Fig. 6.15 (e) shows rotor dynamics during the test. Here, the rotor speed adjusts to change the operating point of the wind turbine. The tip-speed to wind-speed ratio, λ, changes, and therefore, the power extracted by the wind turbine varies as per the output load demand. High oscillation in rotor speed after every step change in wind has been due to an unoptimized PI controller in the DC motor drive.

The performance of the proposed wind system has been reported as, generator acting as a buffer between wind energy and load. Further, Fig. 6.15 (f) shows the transient power consumption by auxiliary motor in rotating the RS. The average power consumption is nearly equal to one by fourth (25%) of the load supplied.

6.4 Performance of the proposed RWECS under constant wind and variable load

Under stand-alone/weak-grid conditions mostly applicable in remote areas, the variations in load affects the voltage quality of the system. Therefore, any energy system dedicated to

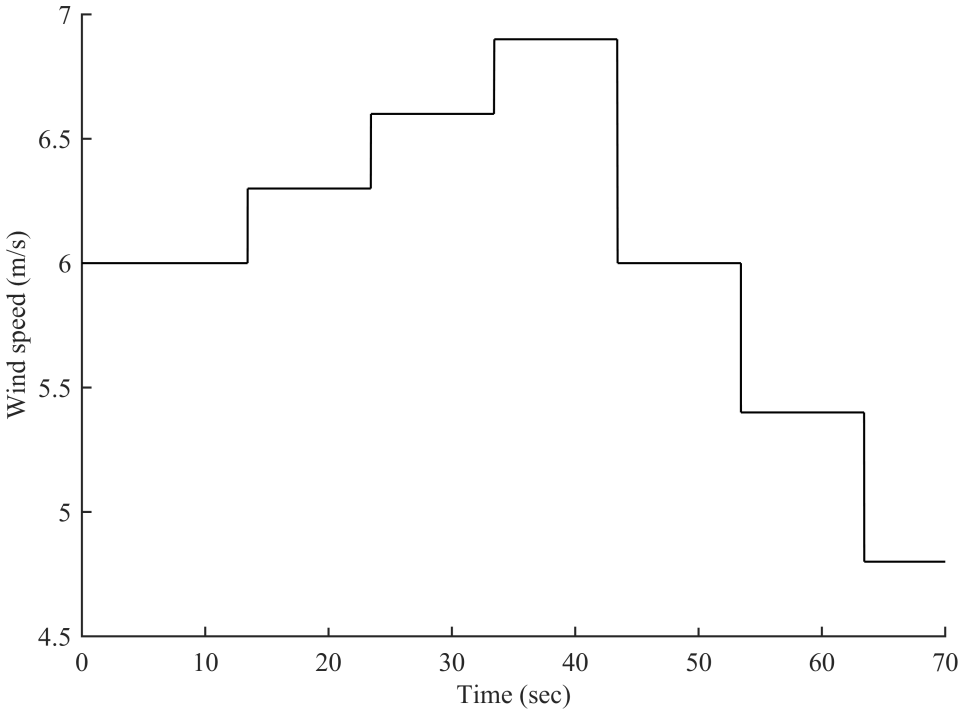

(a) Wind speed profile in the VWCL mode of operation.

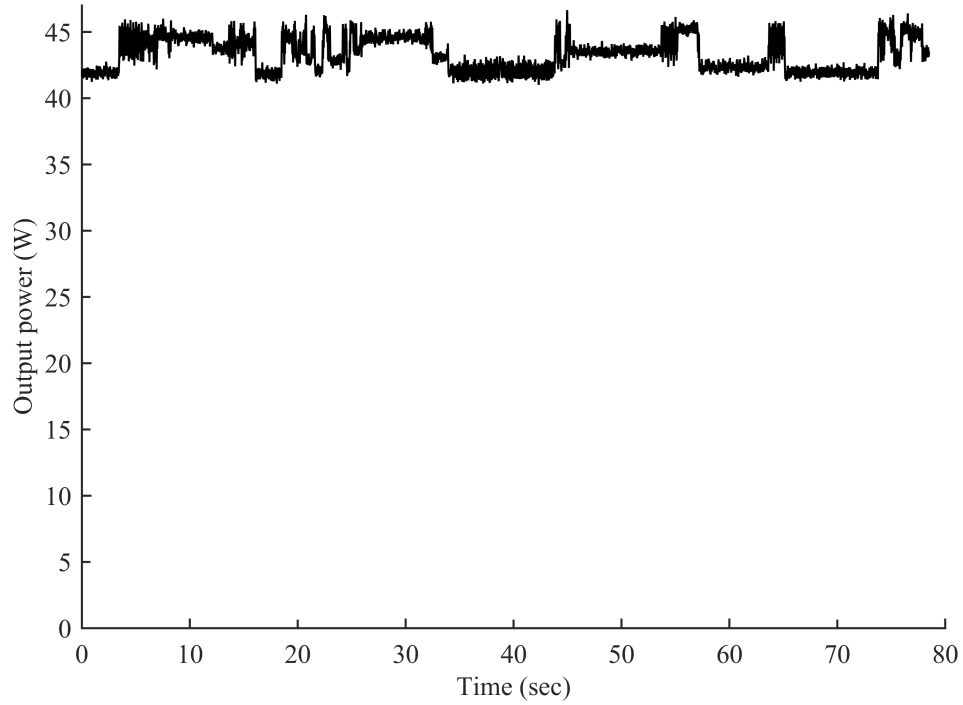

(b) Load profile as per time in VWCL mode of operation

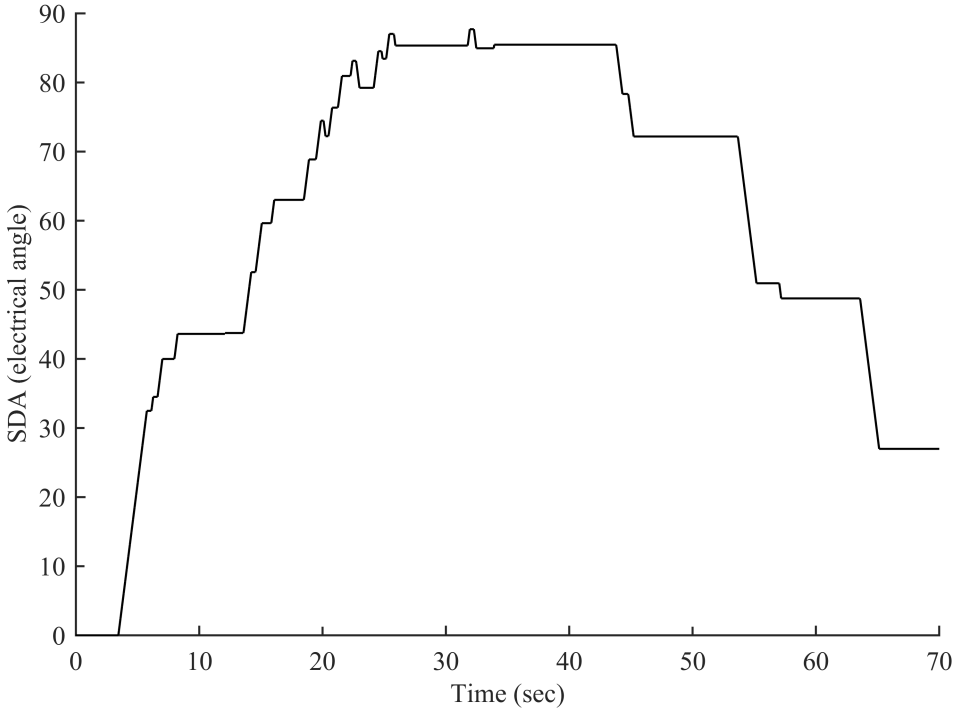

(c) RS angular displacement with respect to SS in electrical degree.

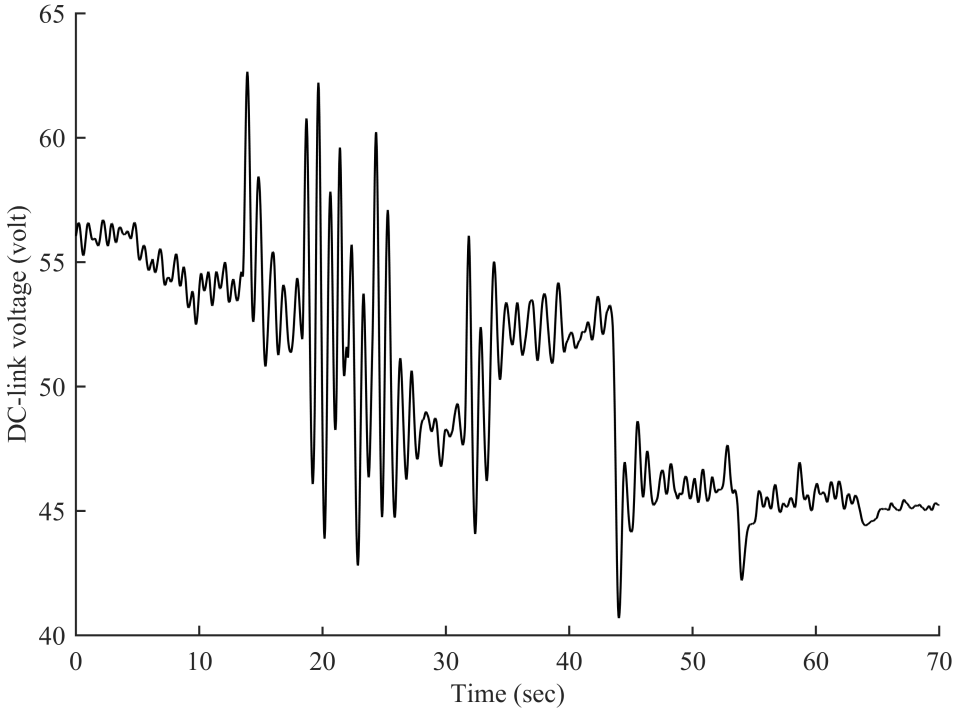

(d) Dynamic regulation of DC-link voltage.

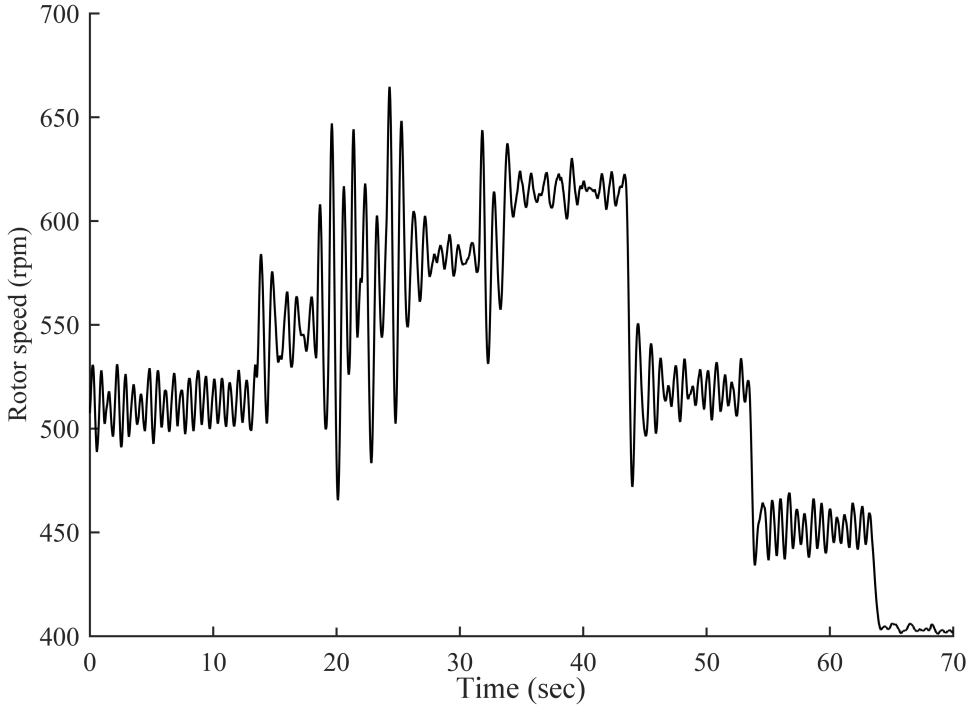

(e) Rotor speed variations as per time in VWCL mode of operation

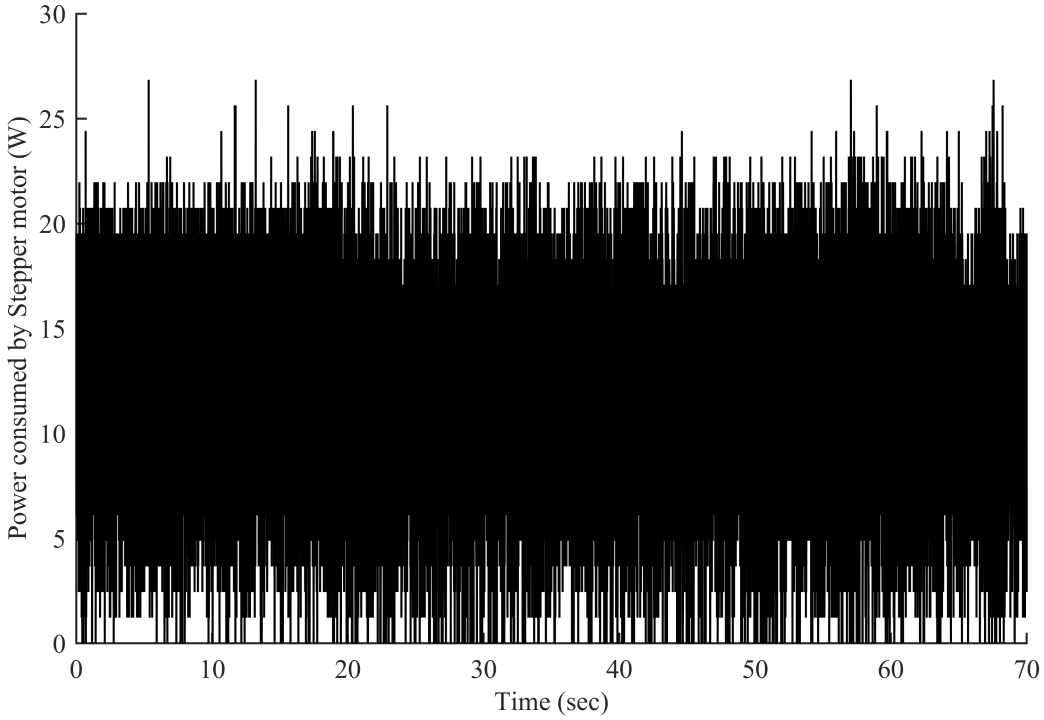

(f) Power consumption by stepper motor while rotating RS

Fig. 6.15 Experimental results on proposed system under variable wind and supplying constant load.

remote areas should be able to counter the intermittent energy source itself as well as for maintaining the output voltage constant invariable to fluctuating loads. Generator voltage regulation capability is tested under constant wind and variable load conditions. The Wind turbine emulator runs at a rated wind speed of 6 m/s. The three-phase Induction motor load varies by changing the three-phase transformer tapping, as explained in section 4.4. Fig. 6.16 (a) presents a typical load profile. Fig 6.16 (b) plots dynamic variation of SDA for controlling the DCV at 50 V. Fig. 6.16 (c) reports the plot of dynamic DCV waveform. For reducing the dc-link ripples (reduced tolerance of DCV) the reference value is made constant, and therefore auxiliary motor has to rotate the RS continuously to maintain the DCV around reference value. The DCV profile can be even more smoothened by using faster actuator or/and reducing RS inertia. Any power shortage/excess in the system due to the variation in the load profile is compensated by using the reserve capacity of the wind turbine, as shown in Fig. 6.16 (d).

6.5 Low-voltage-ride-through (LVRT) capability of the system

LVRT is defined as the sustainability of WECS under grid fault. Under grid fault, grid voltage can go as low as zero before the fault clears. During the fault, the wind generator needs to supply reactive power to the grid for maintaining the voltage at the pre-fault level. As the grid voltage decreases, the ability to inject power into the grid also decreases. Fig. 6.17 shows two systems, in (a) PMSG connects to a healthy grid through a back-to-back converter and in (b) a grid fault is considered in the same configuration. During grid fault, grid voltage dips by V_{dip} pu. Consequently, active power injected in the grid decreases by the same proportion. However, the wind turbine extract power at the prevailing wind speed. Thus, the DC-link capacitor absorbs the excess power in the system. Therefore,

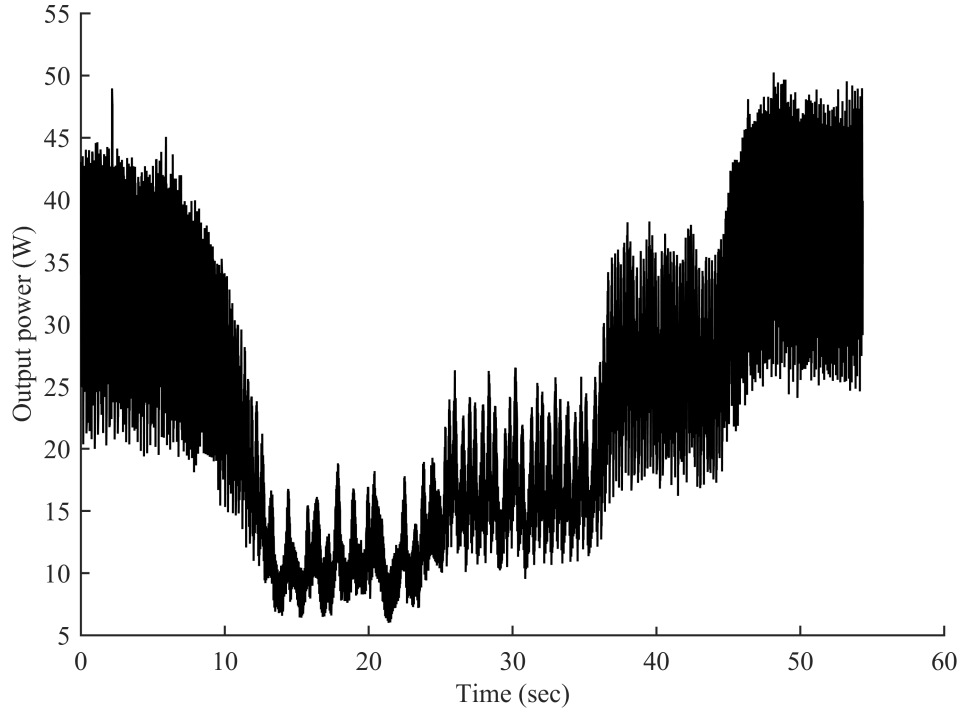

(a) Load profile as per time for CWVL mode of operation.

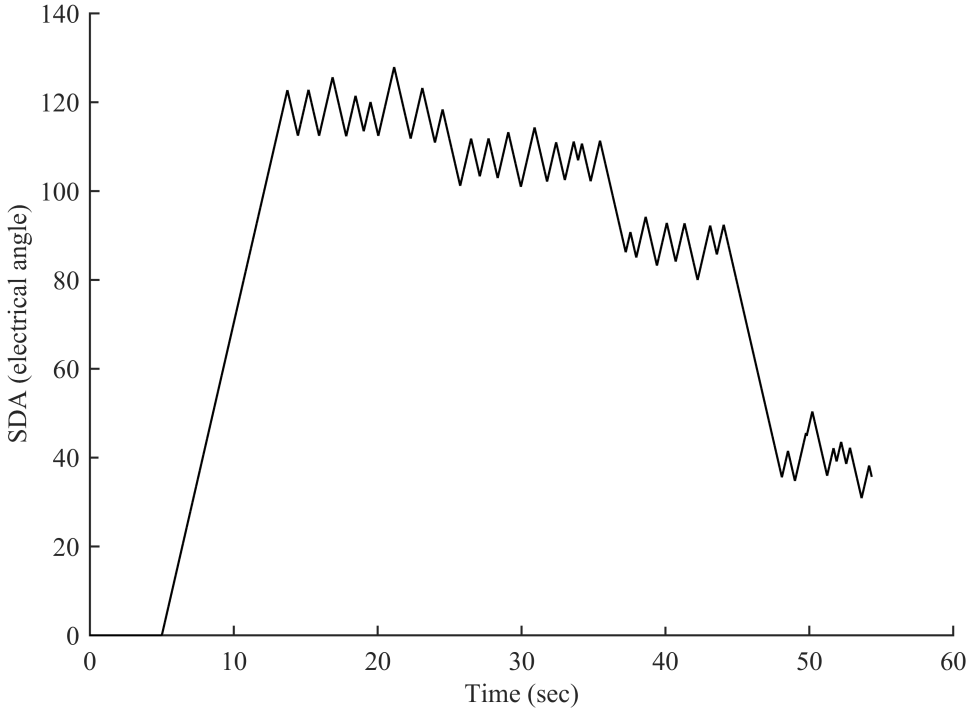

(b) RS angular displacement with respect to SS in electrical degree for CWVL mode of operation.

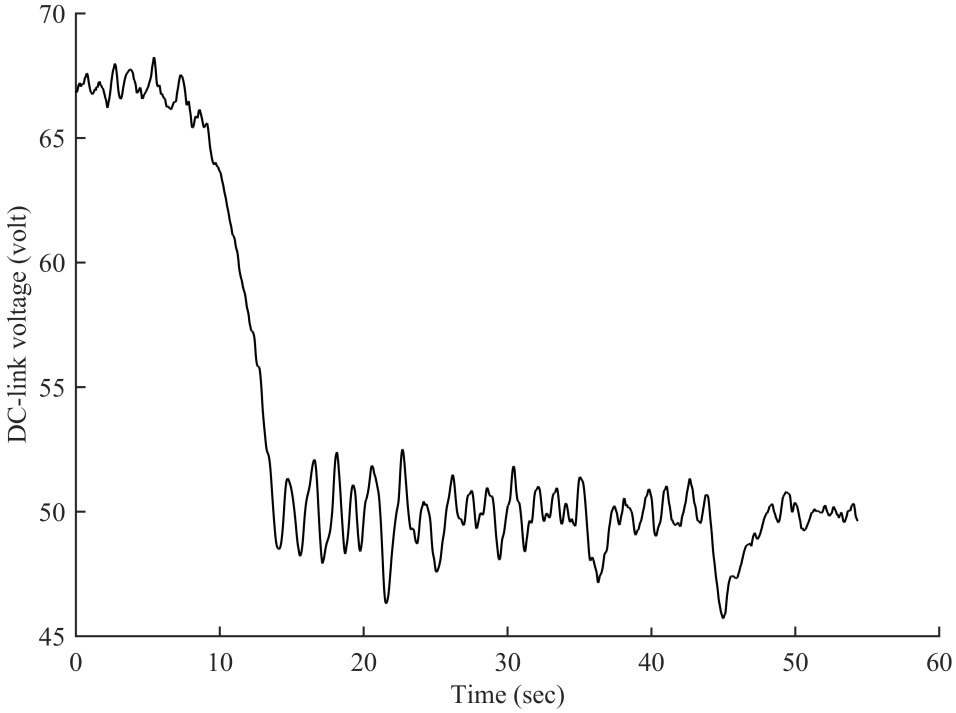

(c) Dynamic regulation of DC-link voltage for CWVL mode of operation.

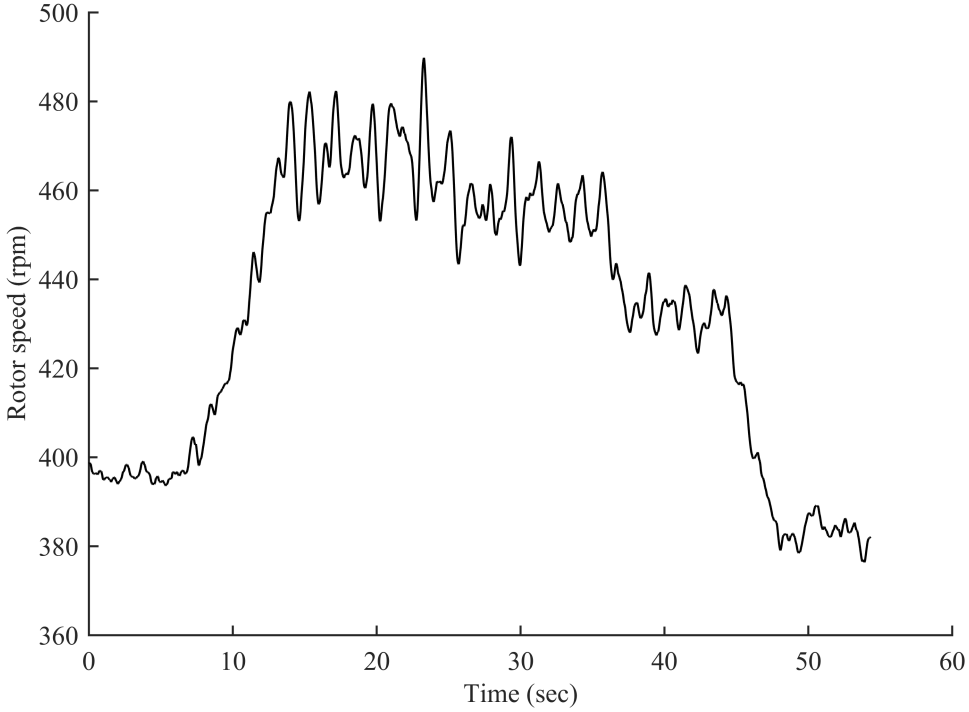

(d) Rotor speed variations as per time in CWVL mode of operation.

Fig. 6.16 Experimental results on proposed system under constant wind and supplying variable load.

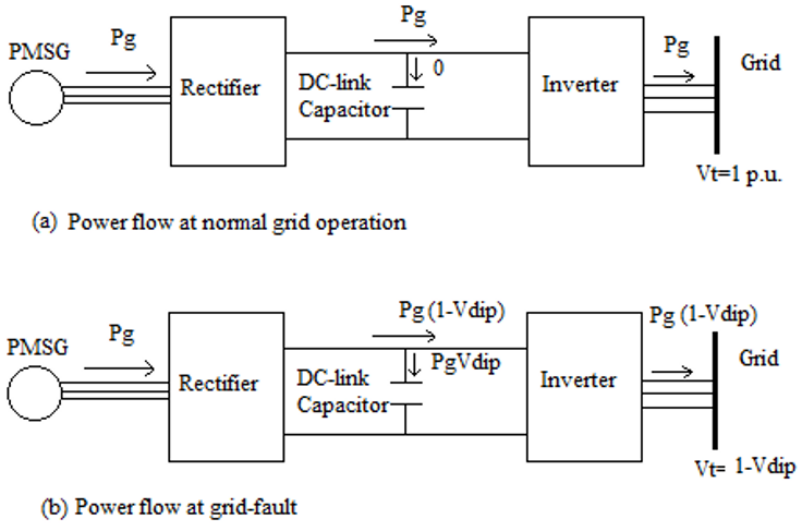

Fig. 6.17 Schematic diagram showing the effect of grid-fault on the system.

DCV increases dangerously, endangering the sensitive power electronic switches in the inverter.

A system with excellent LVRT capability would be able to control the active power flow in the system and generate reactive power to support the grid. Many techniques are proposed to control the surplus active power in the system. The control techniques are fundamentally based on two methods those are as follows

1. Active power control from the wind turbine side

   (a) Turbine Blade Pitch Angle (BPA) control[150].

   (b) Turbine yaw control[29].

   (c) Generator speed control[88].

   (d) Storing surplus energy in rotor[87].

2. Dissipating surpulus energy from the DC-bus

   (a) Electronic switch controlled resistance across DC-bus[149].

   (b) Putting DC-load at DC-bus

The effectiveness of turbine pitch and yaw control is constrained by the maximum rate of pitching angle mechanically possible [150]. Further, the Generator speed control is a smart way to control the active power though the control mechanism is complex and incur higher losses due to use of active generator-side converter. On the other hand, inclusion of braking resistance across DC bus is impractical due to need of high capacity resistances and dissipating heat from it. Storing surplus energy in rotor is very effective, though active generator-side converter is still required.

In summary, the wind generator needs to behave very near to a conventional synchronous generator. Grid codes published by many countries have seen low-voltage-ride-through (LVRT) capability of the generator as the most stringent requirement [149].

In the proposed RWECS, MFW of the generator regulates the active power flow from the wind turbine to the grid. It has the same effect as in the blade-pitch-control method. The advantage of the MFW control technique over blade-pitch control is that no PI controllers are used in the former, and thus the system dynamics are improved.

The Proposed wind system has been tested for a three-phase symmetrical grid fault. In the practical system, a symmetrical grid-fault decreases grid voltage to zero, and thus, active power intake also reduces to zero. The generator is accidentally at no-load upon grid-faults, and a reactive fault current flows in the generator. In the experiments, the wind generator output power is rectified and then filtered through a DC-link capacitor. The DC-link connects to a load resistant through a switch. Unlike in the practical system, the load on the generator is then abruptly disconnected to study the effect of grid-fault. At no-load, the real power supplied by the generator is zero. Here, it is assumed that the reactive power is being controlled at the inverter end. Thus, the experimental setup, as discussed above, can be used to study the active power transients at the time of grid-fault [151].

For testing the proposed system in extreme conditions the fault time has been taken as 2 sec (it could be done as the reactive fault current is zero in the generator). Fig. 6.18 (a) shows V_{DC}, at load condition as well as fault without any controller in action. The voltage dips from 90 volt to 50 volt when the machine is loaded and surges back to 90 volt at fault. During experimentation with controller the rated load voltage has been maintained as to be 40 V. Fig. 6.18 (b) presents the voltage dynamics with the turbine BPA controller on the same lines as done by Conrey, J.F. et al. [149]. The BPA control limits the voltage surge to 60 volts. The oscillations observed are due to the PI controller involved and due to second-order actuator model as reported in [149]. Fig. 6.18 (c) gives the result when MFW of generator is incorporated with BPA control. The dynamic response of the system has deteriorated though; the surge voltage has been curtailed to 50 volts at fault. Fig. 6.18 (d) gives the voltage dynamics with only the MFW controller.

The dynamic and steady-state response has been improved, and surge voltage curtailed to below 50 Volts.

The results give a pessimistic conclusion that the deteriorated dynamic response in the case of all controllers involved is due to the BPA actuator model and PI controller that may not be avoided in the practical system. From the analysis, it is concluded that if the mechanical actuator used for MFW is fast enough in a given system, the LVRT capability of a wind generator can be improved compared to conventional synchronous generator. This ensures a higher penetration of wind generators into the grid.

6.6 Conclusion

In this chapter the experimentations have been performed related to the applicability of the proposed controller in the RWECS operating under varying input wind energy and as well as the output variable load. The results support the hypothesis that the proposed system is a dedicated system for wind energy conversion at locations incurring high wind

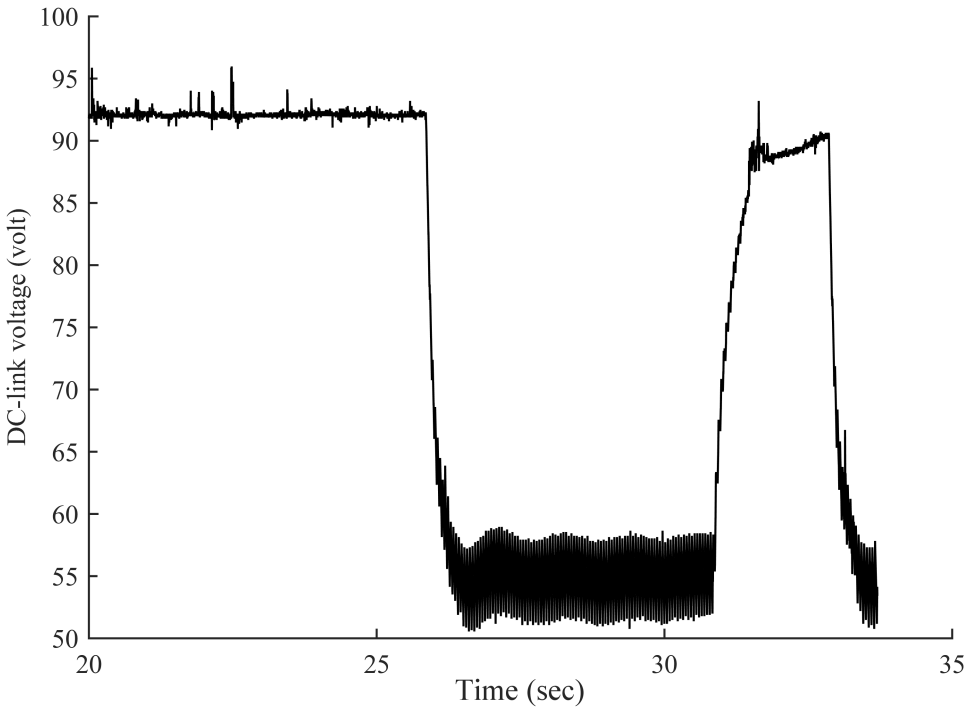

(a) Without controller.

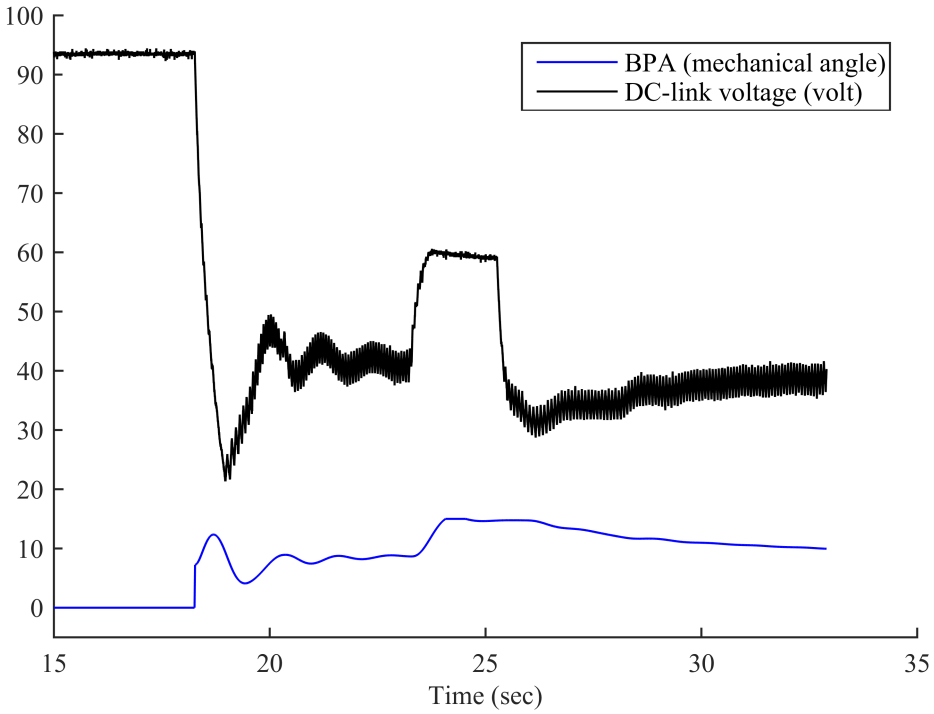

(b) With BPA control

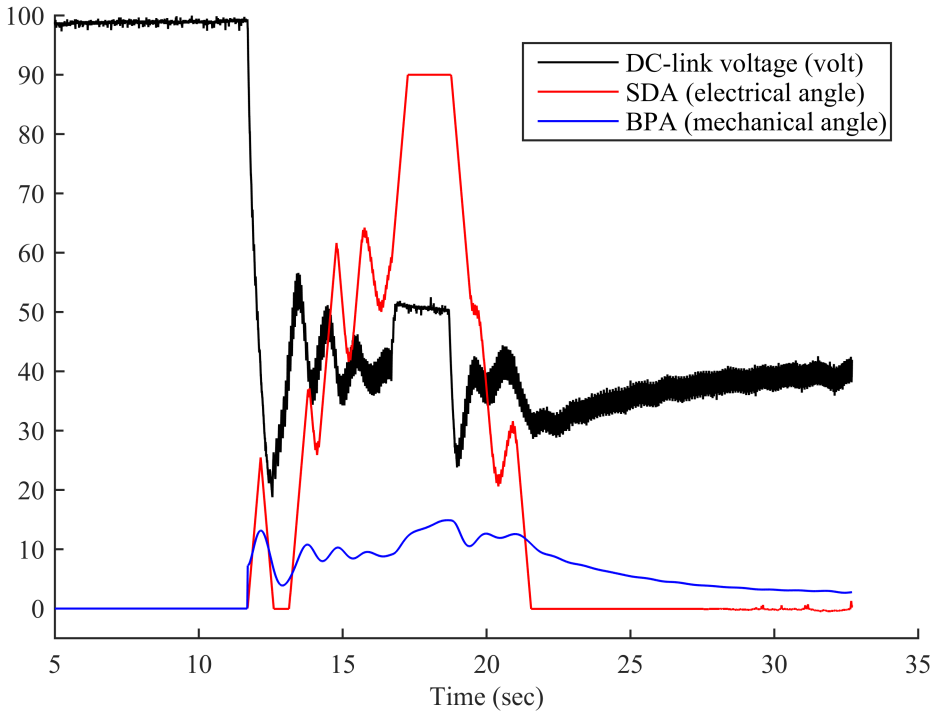

(c) With BPA and MFW control.

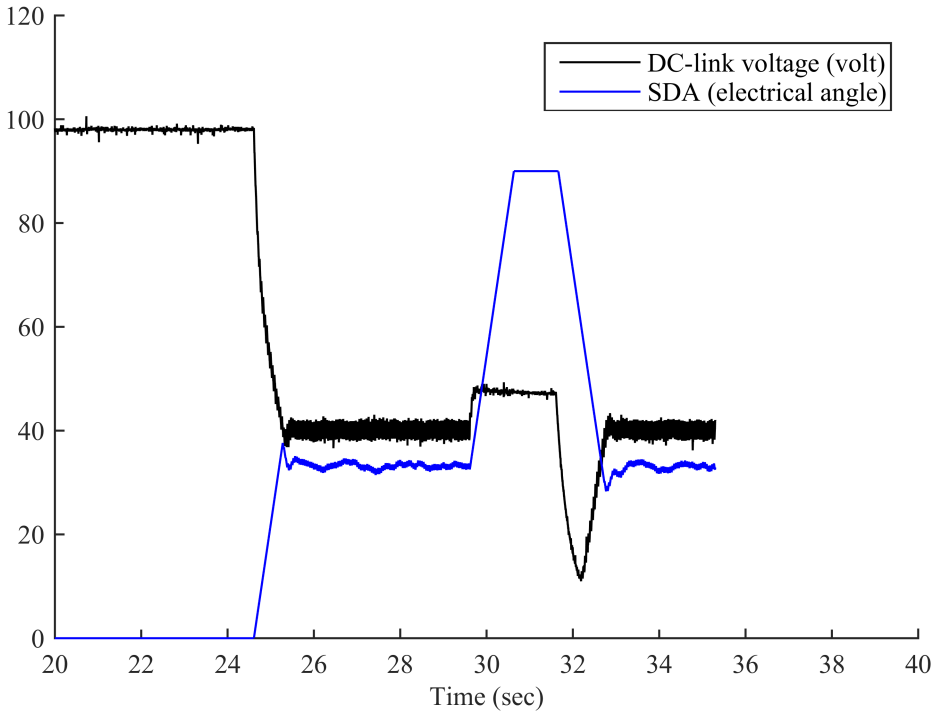

(d) With MFW control.

Fig. 6.18 V_{dc} voltage dynamics at fault.

intermittency, such as at rooftops. Also, the LVRT capability of the proposed system has been checked for a higher level of penetration into the grid.

Thus, it is inferred by experimentation that the current system has high potential in weak-grid/standalone systems owing to its inherent ability to absorb any change of energy, may it be at the input side or output side. This inherent ability of the generator, acting as a buffer between wind energy and load, lets the system work at constant voltage and frequency invariant to any variations in wind speed or/and load.

The next chapter extends the inference derived from the experimentations in this chapter to hybridize the RWECS with rooftop solar energy conversion system. In the next chapter, a rooftop hybrid wind-solar conversion system has been discussed that uses the complementary nature of wind and solar energy conversion systems. A cost-effective solution is proposed that uses minimum capacity of power electronics and energy storage devices that improves the applicability of the system in remote areas.